Heat and Mass Transfer
https://doi.org/10.1007/s00231-020-02812-1

ORIGINAL

Characterization of net coolant flow rate to copper boiling surfaces using two-phase particle image Velocimetry and dielectric fluid

M. Harrison[1] · A. Moita[2] · J. Gess[1]

Received: 13 April 2019 / Accepted: 6 January 2020

Abstract

Particle Image Velocimetry (PIV) has been widely used in fluid mechanics for various single and two-phase flow visualization studies. Using PIV, the net coolant flow rate required for quenching a copper circular heated surface under high heat flux pool boiling applications was quantified. The flow rate was calculated using a control surface analysis of all the periphery vectors surrounding the pool boiling activity. The vectors were deconstructed into their relevant Cartesian components using a custom Matlab code. The acquired data may be useful for empirical modeling of many practical high-performance electronic systems including thermosiphons and multi-component liquid immersion cooled servers. Boiling heat transfer fluxes ranging from 5.5 W/cm^2 to 11 W/cm^2 yielded quenching fluid flow rate requirements ranging from 1.7 g/s to 93.6 g/s. The highest heat flux tested, 11 W/cm^2 is near the Critical Heat Flux (CHF) for the PF-5060 working fluid with a resulting maximum heat transfer coefficient of 8.8 kW/(m^{2}K). With subcooled boiling conditions, it was found that as little as 2.5 °C reduction in pool temperature below the saturation point resulted in a 42% reduction in required coolant flow rate. A further reduction in the cooling flow rate requirement, 87% below the saturated pool condition, was found when the subcooling level was increased to 5 °C. When subcooling is introduced, transient conduction near the microlayer vapor/surface/liquid interface of bubble formation begins to be the dominant heat transfer mechanism.

1 Introduction

According to the 2015 International Technology Roadmap for Semiconductors (ITRS), "microfluidic cooling (single/two-phase)" will be the long-term solution to avoid overheating issues in high heat flux electronic components [13]. By 2024, vertically stacked chips and memory will be prominent, termed "the end of the 2D domain," due to photolithographic, economic, and physical constraints [13]. In specific cases of energy-dense data center installations, system air cooling is reaching its limit [17]. Reviewing Newton's Law of Cooling shows that in order to maintain thermal resistance levels (i.e. chip operating temperature) at increased flux, the heat transfer coefficient must increase for reliable long-term operation. Fortunately, two-phase cooling provides the necessary heat transfer coefficients that are orders of magnitude greater than those produced by conventional air-cooling techniques [2, 25]. Even though two-phase cooling has the potential to meet the future demands of industry/consumer needs, they have not been widely implemented and accepted as a viable solution. Up to this point, the perceived danger in boiling volatility and concern with material compatibility with widely used electronic components has kept this solution from gaining more of a technological foothold. The former is being targeted in this work by using two-phase Particle Image Velocimetry (PIV) to quantify the required quenching fluid flow rate requirements to the boiling surface and showing that these values follow fundamental and predictable trends over a practical working range of heat fluxes leading up to the Critical Heat Flux (CHF). The coolant flow rate requirements acquired using this technique will allow for energy dense surfaces, those with high enough heat fluxes to induce boiling, to be modeled as a hydrodynamic liquid sink. Reducing the complex activity of two-phase heat transfer into an easily implemented boundary condition based on the requisite net mass flow rate will facilitate more economical reduced order modelling of fluid flow around a volatile boiling surface. Knowing how fast and where the liquid coolant flows will allow

✉ M. Harrison
harrism3@oregonstate.edu

✉ J. Gess
Joshua.gess@oregonstate.edu

[1] Department of Mechanical Engineering, Oregon State University, Corvallis, OR, USA

[2] Center for Innovation, Technology and Policy Research, Instituto Superior Tecnico, Universidade de Lisboa, Lisboa, Portugal

Published online: 23 January 2020

designers to remove hydrodynamic impediments to the boiling activity and design better boiling enhancement coatings/microstructures. Ultimately, this method could be developed into a test standard for boiling enhancement surfaces so that any two-phase heat transfer activity can be placed in a hydrodynamic model for the determination of ambient coolant flow around high heat flux boiling activity. Material compatibility with dielectric fluids will not be addressed in this study, but previous work has shown that plasticizer content must be orders of magnitude higher than anticipated exposure levels before fully-developed heat transfer is negatively impacted [23].

Pool boiling heat transfer is known to remove high heat fluxes through three main mechanisms: forced convection, latent heat (through bubble formation) and the so-called quenching heat transfer, resulting from the rewetting and rebuilding of the thermal boundary layer after bubble detachment (e.g. [10, 16]). Based on an approach with strong empirical underpinnings, many authors emphasize the relative dominance of the latter (e.g. [6]) while others (e.g. [27, 28]) advocate for alternating dominance of different mechanisms, depending on the working conditions. The results obtained in the present study establish the dominant heat transfer mechanisms in a quantitative way.

This study measures the quenching fluid flow rate of the boiling process to a bare circular copper disk using PF-5060 as the working fluid, a common dielectric fluid for liquid immersion cooling applications, under saturated and subcooled conditions. The results have shown the fundamental expectation that quenching fluid flow rate requirements increase with increasing heat flux. This is especially apparent under saturated pool conditions where transient conduction as a heat transfer mechanism is not as prevalent. Having the ability to control the bulk fluid temperature at such a high resolution, the chamber maintains a temperature uniformity across the entire pool of ±0.5 °C. Experimentation has shown that transient conduction has a drastic effect on the overall net coolant flow rate under subcooled boiling conditions [11]. When the bulk fluid temperature is maintained at 2.5 °C and 5 °C below saturation temperature (56 °C at 1 atm) the net coolant flow rate is substantially reduced by 42% and 87%, respectively, due to an increase in thermal potential across the conduction thermal boundary layer at the boiling surface. Uncertainty in the net coolant flow rate was 11.6 g/s and 0.9 g/s at the highest and lowest heat fluxes, respectively.

2 Literature review

Previous work in two-phase PIV was primarily performed with water due to an inability to find a density-matched fluorescent particle that is compatible with the heavier dielectric fluid utilized in this study. Investigating previous works with water shows that various flow visualization techniques such as combinations of multi-camera setups, shadowgraphy, and seeding configurations have been used for two-phase flow characterization [24]. Permutations of experimental configurations presented in this review [24] centered on the requirements of contrasting the vapor from the liquid phase. In a previous work by the same authors [8] the contrast was provided by a rhodamine B coated particle with a specific density of 1.51 g/ml, which is near the 1.6 g/ml of the dielectric used for two-phase immersion cooling. The same particles and density matching were also used in the current study. In the previous study by Gess et al., a quad-socket board with a 2 × 2 array of 1″ × 1″ (25.4 mm × 25.4 mm) heated elements were used to simulate high performance processor chips commonly used on data server motherboards. Utilizing FC-72 as the cooling agent, two-phase heat transfer was initiated with heat fluxes as high as 11 W/cm^2 from a bare silicon surface. In that study [8], the ability to capture every vector flowing into the surface was limited due to the confinement of the small form factor Line-Replaceable Unit (LRU) server examined. More specifically Gess et al. were unable to quantify the vectors facing normal to the boiling surface, arguably the most important when considering a net coolant flow rate calculation. However, even with the mentioned limitations, it was shown that increasing heat flux resulted in increased flow rate to the surface [8]. As the boiling becomes more vigorous and vapor generation increases, the surface requires a higher flow rate of coolant to quench the surface to prevent burnout. The experimental facility used in the current study was constructed with optical access as the primary design feature, facilitating the visualization of the vectors facing normal to the boiling surface.

Particle Image Velocimetry (PIV) first appeared in literature in 1984, and it is defined as the accurate, quantitative, and simultaneous measurement of fluid velocity vectors within a prescribed Field of View (FOV) [1]. PIV examines the motion of illuminated particles seeded in a moving fluid over a known time step. The displacement of these particles between two successive images is related to the velocity by the known sequential time-step. The particles selected for this study are Rhodamine B coated microspheres of 1 μm in diameter. An Nd:YAG laser, with an excitation wavelength of 532 nm, fluoresces a light signature from the particles of 584 nm. A high-pass filter allows the fluorescing light to enter the camera's Charge-Coupled Device (CCD) but removes the excitation laser emitted from the laser. The result is an image, like that shown in Fig. 1, where reflection of green laser light from rising vapor is removed for subsequent PIV analysis. Previous work by Westerweel concluded that fluid motion characterization is improved through higher spatial resolution [29]. During the previous study by the same authors [11], the net coolant flow rate was quantified using PIV and 4-μm diameter particles. In an effort to improve upon the previous results, this current study uses 1-μm diameter particles to

Fig. 1 Typical image captured by camera/filter/laser system showing particles are the only items illuminated

achieve four times the spatial resolution while analyzing the same optimal FOV determined analytically in the previous work by the same authors [11]. This was done to minimize the effects of slip velocity induced by increases in particle diameter from 1 μm to 4 μm which was calculated to be 105 nm/s and 1.2 μm/s, respectively.

3 Experimental facility

3.1 Boiling chamber

During experimental facility design there were three major areas of concern; the ability to have a 360° view of the boiling surface, ability to control bulk fluid temperature at a high spatial resolution, and control of the entire bulk fluid temperature to within 0.5 K. Fig. 2 shows a 3D model of the facility utilized during the experiment. The left image of Fig. 2 shows a section view where many of the internal components used for spatial control of the temperature within the pool surrounding the test surface are visible. The boiling chamber itself is 190 mm × 190 mm ×152 mm (W x D x H) with 85 mm × 85 mm square quartz windows on each side. These windows allowed for an unobstructed view of the boiling surface during experimentation and allowed for the laser sheet to exit the facility cleanly, preventing any interference or reflection from the back plane of the test chamber. The chamber holds roughly 5.5 l of PF-5060, the working fluid, and was filled to 80% capacity during experimentation. Many boiling studies use one thermocouple placed in a quiescent area within the pool to measure the ambient fluid temperature. However, the current study uses four Type-K thermocouples strategically placed in feedback-loop controlled zones surrounding the boiling test surface. Each thermocouple was placed 46 mm from the edge of the boiling surface and 51 mm from their respective condensing coils. This increased fidelity is needed to make claims regarding the effect of minimal changes in subcooling conditions, as little as 2.5 °C. This approach yielded spatial uniformity throughout the pool of less than ±0.5 °C. The thermocouples were placed far enough away from the boiling activity so as to not disrupt quenching fluid flow paths. These thermocouples were calibrated against a thermistor with a NIST-traceable uncertainty of 0.2 K within an insulated lab-grade oven.

To achieve pool temperature uniformity, a mixture of four cooling coils, eight resistance heaters, and a LabVIEW

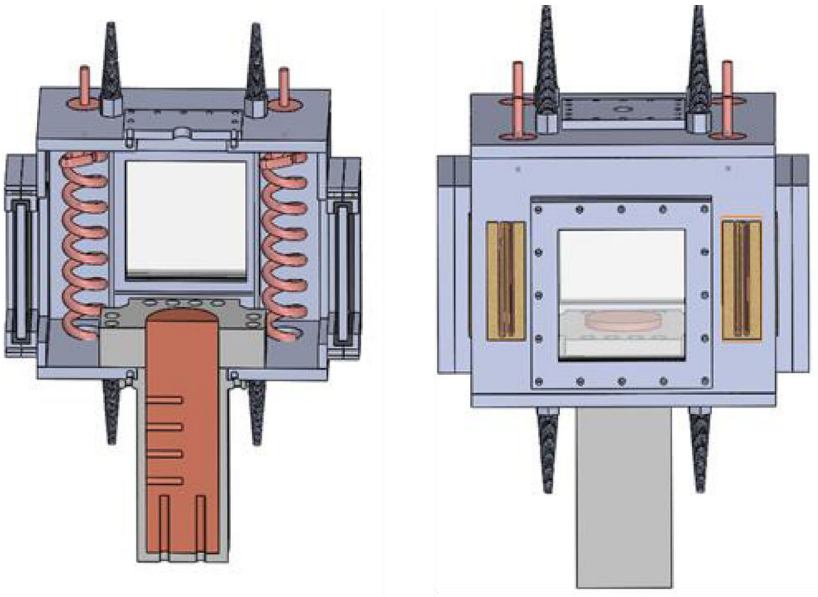

Fig. 2 3D Solidworks model - a) Section view of experimental facility. b) Side view of experimental facility

a) b)

program were implemented. Figure 3 displays the flow loop for the chilled water and placement of heaters/thermocouples in the facility design. For heating the bulk fluid temperature, eight Kapton resistive heaters were placed on the outside of

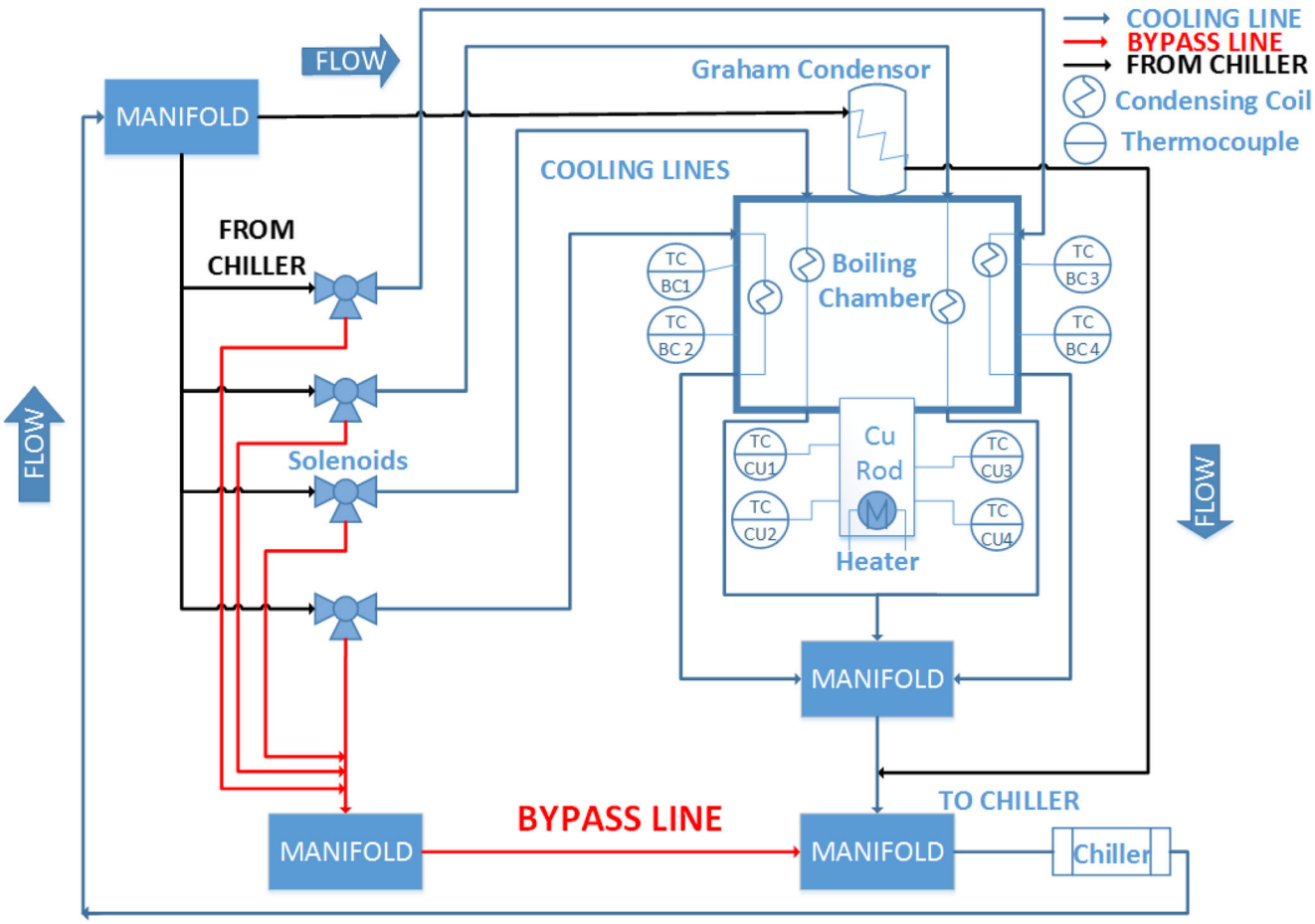

Fig. 3 Flow Schematic for experimental facility

the facility, two on each wall on both sides of the viewing window. A 2500-W chiller was used to supply chilled water to the Graham condenser and each of the cooling coils that were inserted in each corner of the chamber. A Graham condenser was used to maintain atmospheric conditions within the chamber during all of the pool boiling experimentation conducted. A solenoid valve was placed upstream of each cooling coil to regulate flow depending on in situ pool temperature readings.

Precise control was necessary to maintain pool temperature uniformity with minimal uncertainty. This was achieved by splitting the boiling chamber into four zones, which are pictured in Fig. 4. The feedback control loop was managed through an in-house LabVIEW VI. By indicating desired maximum and minimum temperatures, each thermocouple readout would open the corresponding solenoid valve to cool the corner, turn on the heaters to raise the temperature, or bypass the flow and turn off the heaters once the zone reached steady state under the desired pool conditions. Using a time-averaged result from the thermocouple output over 30 s, each zone could be controlled within the desired 0.5 K temperature range.

3.2 Boiling surface

The boiling surface was made from a single 50.8 mm diameter rod of copper 110. The motivation for this was to eliminate contact resistance between a separate surface structure and the heating element, thus increasing overall accuracy of the surface temperature and heat transfer coefficients measured. The overall length of the rod was 167 mm. The smooth surface was polished using a series of silicon carbide sand paper from 200 to 4000 grit. After obtaining a mirror-like finish with the 4000-grit sheet, the surface was then polished and cleansed with PF-5060 to remove all contaminants left over from the polish. The rod was heated uniformly by using four 6.35 mm diameter and 38 mm tall cartridge heaters equally placed in a 25.4 mm diameter circle. Each heater was press fit into the bottom of the rod. The power was controlled by a TDK Lambda 10 kW power supply. The internal temperature gradient was measured using four 76 mm long K-type sheathed thermocouples. Each thermocouple was inserted 25.4 mm into the center of rod and placed at locations 53.5, 72.5, 91.5, and 110.6 mm from the surface. Each thermocouple was calibrated with the same technique used for the pool thermocouples discussed in the Boiling Chamber section. Using the least squares method, a linear equation was calculated, and the surface temperature was determined using the known distance from the heaters and linear extrapolation of Fourier's Law. To ensure ambient heat loss was negligible, the copper rod was insulated using a Delrin carriage.

3.3 Uncertainty analysis

A Kline McClintock uncertainty analysis [18] was performed to validate that this measurement technique would be within a usable range. The q" and h are the two parameters of interest. These will be used to validate this experimental facility against previous work. Equations 1 and 2 display the methodology in which the uncertainty was calculated.

$$U_{q''} = \sqrt{\left(\frac{\partial q''}{\partial V} U_V\right)^2 + \left(\frac{\partial q''}{\partial I} U_I\right)^2 + \left(\frac{\partial q''}{\partial A} U_A\right)^2} \quad (1)$$

$$U_h = \sqrt{\left(\frac{\partial h}{\partial q''} U_{q''}\right)^2 + \left(\frac{\partial h}{\partial A} U_A\right)^2 + \left(\frac{\partial h}{\partial T_{surf}} U_{T_{surf}}\right)^2 + \left(\frac{\partial h}{\partial T_{Bulk}} U_{T_{Bulk}}\right)^2} \quad (2)$$

Table 1 depicts the calculated uncertainties for the highest and lowest heat fluxes for each pool condition. It was found that the surface temperature uncertainty remained constant under various heat fluxes. The heat flux uncertainty was minimal due to the high precision machining of the copper rod and the uncertainty in the current and voltage being 0.3% and 0.1% of the readings respectively. This resulted in minimal uncertainty with the heat flux. The heat transfer coefficient uncertainty averaged 3.5% over all the data points.

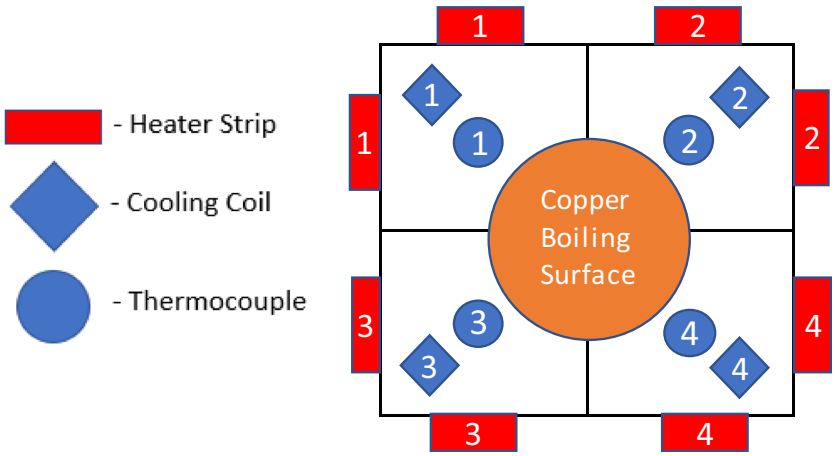

Fig. 4 Illustration of each zone in which the boiling chamber was split

Table 1 Uncertainty Values for vital experimental parameters

q"(W/cm2)	Saturated		2.5.° Subcooled		5° Subcooled	
	11	5.5	11	5.5	11	5.5
Thermocouples (°C)	0.2	0.2	0.2	0.2	0.2	0.2
TSurface (°C)	0.4	0.4	0.4	0.4	0.4	0.4
TBulk (°C)	0.2	0.2	0.2	0.2	0.2	0.2
Area (cm2)	2.03E-02	2.03E-02	2.03E-02	2.03E-02	2.03E-02	2.03E-02
Current (mA)	8.7	6.2	8.7	6.2	8.7	6.2
Voltage (mV)	77	55	77	55	77	55
q"(W/cm2)	0.04	0.02	0.04	0.02	0.04	0.02
h (W/m2K)	301	160	230	108	146	72.66

3.4 Net coolant flow rate error

The error associated with calculation of the net coolant flow rate was found by implementing a standard error mean approach. Equation 3 was used to calculate the error. Where σ is the standard deviation and n is the total number of samples taken for each steady state data point. Tables 2 and 3 summarizes the error over the full range of heat fluxes and pool conditions for saturated and subcooled pool conditions respectively.

$$\sigma_x = \frac{\sigma}{\sqrt{n}} \tag{3}$$

Table 2 Standard Error of Net Coolant Flow Rate Under Saturated Pool Conditions

HEAT Flux (W/cm2)	Saturated Error(g/s)	Saturated %Error
5.5	0.90	53.0%
6	0.80	32.6%
6.5	1.75	30.4%
7	1.73	34.2%
7.2	2.39	30.3%
7.4	2.81	39.6%
7.6	3.63	31.0%
7.8	5.04	26.7%
8	5.36	31.0%
8.2	5.71	24.5%
8.4	6.96	27.6%
8.6	6.91	19.9%
8.8	7.12	19.3%
9	9.19%	20.4%
9.5	9.38%	19.5%
10	10.59%	18.0%
10.5	10.31%	16.7%
11	11.67%	12.5%

3.5 PIV measurements: Set-up and procedures

A LaVision PIV suite was utilized for data acquisition and analysis. Particles 1 μm in diameter, coated in Rhodamine B, were used for tracking. A new wave SOLO PIV Nd:YAG laser was placed 500 mm from the area of interest. A 1 mm laser sheet was projected through the center of the boiling surface. Images were captured using LaVison's Imager sCMOS camera (2560×2160 pixels^2) with a 545 nm high pass filter blocking all visible light that was not illuminated by the laser particle interaction. The time delay between laser pulses was held constant at 5 ms for all experiments. Forty consecutive image sets were captured at a rate of 25.744 Hz. A typical image captured by this setup can be seen in Fig. 1. Analysis was performed using DaVis 8.4 software. A cross correlation algorithm with decreasing window sized was used for the PIV image analysis. Starting with a 128×128 pixel window with 50% overlap and two passes, it was then reduced to a 64×64 pixel window with 75% overlap and three passes. The resultant velocity profiles were then run through a non-linear filter eliminating any erroneous vectors within the image. Finally, an average was taken for all forty image sets. Figure 5 shows the typical velocity vector map after post processing.

3.6 Experimental facility validation

Previous work [20] was used to show that data yielded from the current experimental facility was matching expected fundamental results. In Parker's study, FC-72 was used as a working fluid which has the same boiling characteristics as the PF-5060 coolant used in this study. Table 4 is a condensed comparison of the thermophysical properties of the PF-5060 coolant used for the current study and the FC-72 fluid used for experimental validation. All of the data was obtained from 3 M's material safety data sheets for each fluid, and the relative variance in properties maintains continuity with increased fluid temperature.

Table 3 Standard Error of Net Coolant Flow Rate Under Subcooled Pool Conditions

Heat Flux (W/cm2)	5° Subcooled % Error(g/s)	5° Subcooled % Error	5° Subcooled % Error(g/s)	5° Subcooled % Error
5.5	0.25	33.8%	0.35	19.2%
6	0.28	25.7%	1.00	21.2%
6.5	0.30	45.4%	1.10	28.3%
7	1.54	23.6%	0.24	13.0%
7.5	2.11	20.8%	1.66	23.9%
8	2.76	26.5%	0.54	16.1%
8.5	3.36	23.4%	0.94	22.0%
9	2.95	21.8%	0.96	19.1%
9.5	3.35	22.9%	0.56	14.7%
10	3.74	25.4%	0.62	19.4%
10.5	4.18	28.4%	0.58	19.7%
11	3.42	26.5%	1.08	17.1%

Parker's work examined fluxes over the entire boiling curve, as it was focused on developing fundamental characteristics of boiling performance, while the current study focuses on a heat flux range where boiling activity is sufficient enough to induce measurable and practical net coolant flow rates. Figure 6 shows that our results correlate well to the data reported by Parker when comparing heat flux with respect to heat transfer coefficient. Heat transfer coefficients were calculated based on the extrapolated surface temperature process, as explained in Section 3B, and the ambient pool temperature measured at each feedback-controlled zone within the test chamber, as explained in Section 3A, as the driving temperature difference in Newton's Law of Cooling. The heat flux was acquired using the exposed copper surface area in tandem with the heat applied to the surface, calculated by multiplying the voltage and current of the power supply feeding the cylindrical resistors embedded in the base of the copper rod. It is shown that during saturated pool conditions, current data are nearly identical to that of Parker for measured heat transfer coefficients. As is fundamentally expected, data for the 5 °C subcooled pool condition lays nearly half way between Parker's saturated and 10 °C subcooled (10°SC) pool condition data. Current data for the 2.5 °C subcooled pool condition lays halfway between the saturated and 5 °C subcooled pool condition. Intermediate pool conditions between saturation and 10 °C subcooled follow the expected trend that decreased pool temperature increases the pool boiling heat transfer coefficient.

4 Analytical approach

In the current study a control volume around the boiling surface was established to account for all fluid motion travelling

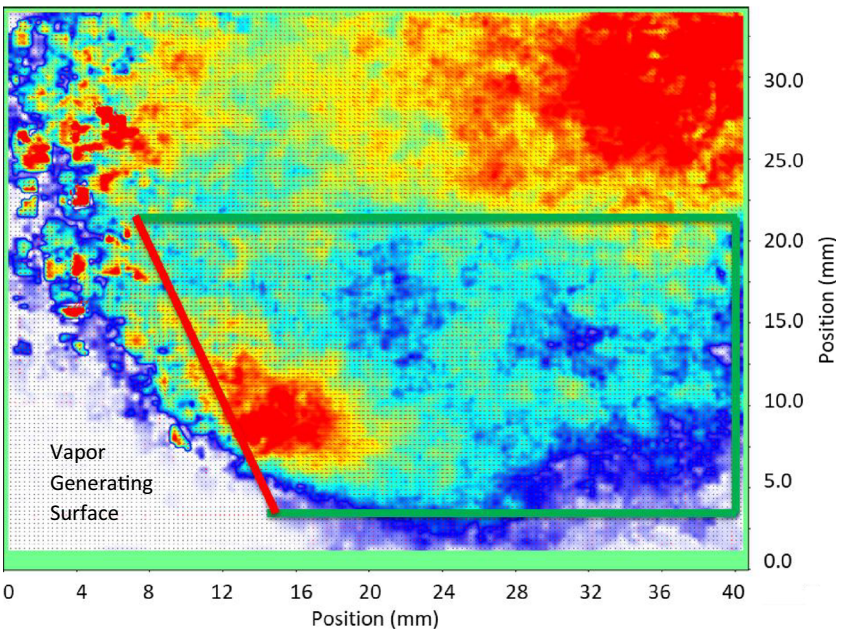

Fig. 5 PIV vector map produced after image processing. Control volume shown and it was assumed all flow in through green lines equals flow out through the red line

Table 4 Main Thermophysical Properties of FC-72 and PF-5060 at 25 °C

Property	FC-72	PF-5060
Avg. Molecular Weight	338	338
Boiling Point (1 atm)	56 °C	56 °C
Vapor Pressure	30.9 × 103 pascals	30.9 × 103 pascals
Latent Heat of Vaporization	88 J/g	88 J/g
Liquid Specific Heat	1.1 J/g °C	1.05 J/g °C
Liquid Density	1680 kg/m3	1680 kg/m3

to the boiling surface. Figure 7 illustrates the general approach of discretizing vectors that were acquired by PIV and how the vector components were applied to the control volume to calculate the net coolant flow rate. Equation 3 was used to calculate this flow rate at each discretized level of the cylindrical control volume. A 2D slice of this control volume is shown in Fig. 5. This control volume was assumed to be axisymmetric around the heating element and fixed in space. In previous work by the same authors, an optimization algorithm was employed to find the best control volume area around the fluid/vapor zone to calculate the net coolant flow [11]. The same FOV established in that work [11] was used as the control volume in the current study with increased spatial resolution due to the implementation of smaller 1-μm diameter particles and a decrease in the initial interrogation window size. The green lines in Fig. 5 correspond to the optimal control volume established in previous work by the same authors [11]. In the net coolant flow rate computational algorithm, the red line is established by connecting the optimally placed terminus of the bottom green line nearest the boiling surface and the terminus of the top green line nearest the boiling activity. The authors acknowledge that a straight line connecting these two points does not represent the curvature of the vapor plume formed. Future work will implement two-color Laser Induced Fluorescence (LIF) to establish a more defined boundary and near field temperature profile to the rising plume. The authors feel however, that the establishment of the boundaries near the boiling surface and at a point near the top of the plume where boiling activity is shown to end is sufficient for the current study. To maintain uniformity, the dz. component was also held constant at 355 μm, corresponding to a 128 × 128 pixel final interrogation window for first pass analysis with a reduction to 64 × 64 pixel final pass. The incoming densities, ρ, were adjusted based on pool conditions; saturated, 2.5 K and 5 K subcooled. The outgoing densities were assumed to have been heated to the saturation temperature for each condition. The net coolant flow rate presented here is the sum total of all the discretized mass flow rates calculated by Eq. 3 over the entire control volume surface.

$$\dot{m}_{m,n} = \rho \cdot dz \cdot \pi \cdot \mathrm{D} \cdot \left(\vec{u}_{m,n} \cdot \vec{n}_{m,n} \right) \tag{4}$$

The experimental error in the net coolant flow rate was calculated by combining the uncertainty in the calibration plate, spatial resolution of the camera, the resulting vector grid array, and slip velocity error. A Single-Sided Single Plane (SSSP) gridded calibration plate was machined in-house with a hole diameter and spacing tolerance of 1.11 mm. The 5.5 MP camera used has a spatial resolution of 0.2 nm/pixel within the 40.2 mm × 32.7 mm FOV examined. With a resulting 2D 135 × 160 vector array in the FOV, the uncertainty in the height of each slice examined, shown as δz in Fig. 7, was calculated to be 11.2 μm. Using the properties provided in Table 5 and Eqs. 5–7, the slip velocity for the 1-μm diameter

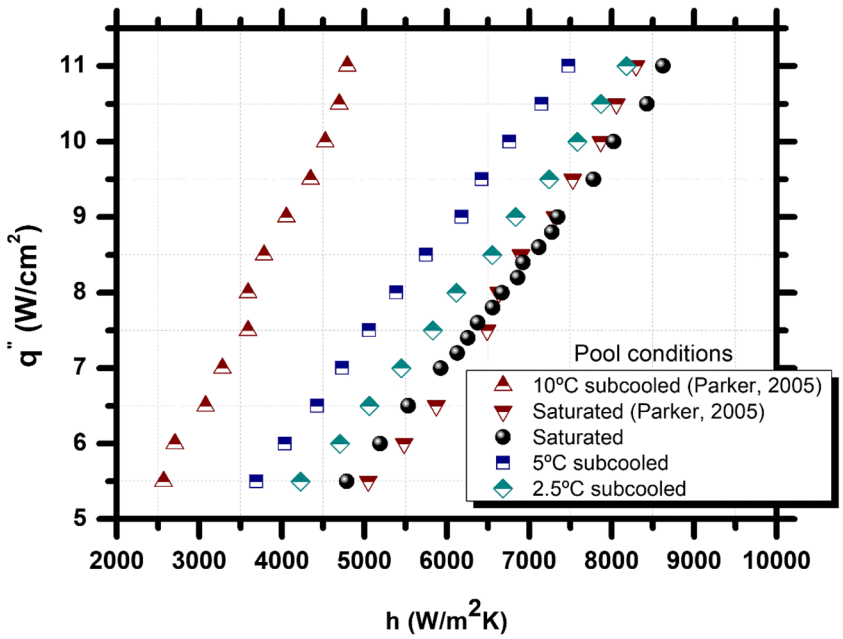

Fig. 6 Comparison of heat transfer coefficients between Parkers experiment (triangles) and current study

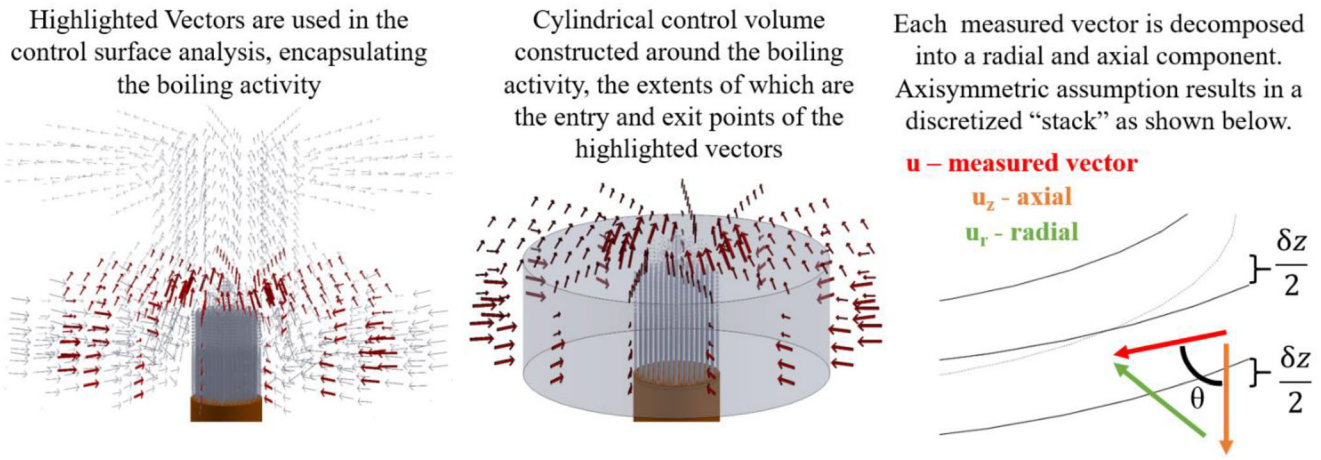

Fig. 7 Diagram displaying control volume and vector decomposition

particle used in this study was calculated to be 105 nm/s. The discretized mass flow rate error associated with Eq. 4 was summed over each vector analyzed for the final net coolant flow rate error. The angle of the vector was calculated at each location using the x and y components provided by the DaVis software. Then, depending on where the analysis was conducted, axial and radial component errors were excluded. For example, for vector analysis around the circumference of the control volume, the axial vector error was excluded. In the analysis for the net coolant flow rate exiting or entering from the top or bottom of the cylindrical control volume, radial vector errors were excluded as these components are not normal to the top and bottom control surface being assessed. The calibration error, camera spatial resolution error, and slip error were all applied to the resultant vector before geometric decomposition into x and y components using the calculated internal angle, , as shown in Fig. 7. Spatial resolution errors were then applied to the diameter of the control volume, D, and the height of the slice, δz.

$$\tau_p = \frac{\rho_p d_p^2}{18\nu_l \rho_l} \tag{5}$$

$$u_s = \frac{\overline{\rho}-1}{\overline{\rho}}\, g\tau_p \tag{6}$$

$$\overline{\rho} = \frac{\rho_p}{\rho_l} \tag{7}$$

Table 5 Properties used to calculate slip velocity error (Eq. 5–7)

Property	Value
Particle Diameter	1×10^{-6} m
Particle Density	1510 kg/m^3
Liquid Kinematic Viscosity	2.7×10^{-7} m^2/s
Liquid Density	1593 kg/m^3
Gravitational Acceleration	9.81 m/s^2

Net coolant flow rate calculations show a dramatic shift in the hydrodynamic and thermal behavior between subcooled and saturated pool boiling conditions. As illustrated in Fig. 6, it was shown that saturated and subcooled data were meeting fundamental expectations for heat transfer coefficients in the partially developed and fully developed boiling regime. Along with validating thermal performance expectations from previous work [20], the present study displays the same trend from previous work by the same authors that increased boiling activity requires a higher flow rate of coolant supply [8]. As one moves up the boiling curve, more nucleation sites become active [12, 3] and, as the number of sites grow, the amount of fluid being vaporized increases. This increase in vaporization will result in the demand for more fluid to quench the boiling surface. Restriction, or an inability for the coolant to reach the boiling surface at this required flow rate, will induce thermal runaway. This experimental technique could be used in a practical application where coolant flow rate requirements to multi-component systems could be modelled and optimized using the net coolant flow rate measurements empirically acquired as a hydrodynamic boundary condition.

The empirical input to an optimization model is arguably more critical in two-phase heat transfer applications than single-phase cooling as there are several parameters that affect general heat transfer performance which are likely to impact net coolant flow rate requirements. For example, microstructuring and fouling over time can have a dramatic effect on boiling heat transfer coefficients. Square surfaces will behave differently than round surfaces due to convergence of coolant flow near the corners. Future work is geared toward modifying the existing experimental facility to quantify empirical data for all of these variables known to affect two-phase heat transfer. The goal of this approach is to provide a standard test procedure for development of empirical data in conventional CFD codes used to optimize energy-dense two-phase thermal management solutions. This study however proves the viability of the technique by confirming

fundamental expectations regarding the need for increased coolant supply at increased power dissipations (shown by the orange saturated pool condition data in Fig. 8) and the impact of subcooling on the dominant surface heat transfer mechanisms (shown by the blue subcooled condition data in Fig. 8).

Subcooling the bulk fluid affects many aspects of the boiling process. It increases the departure frequency, while lowering departure diameter [4, 3]. This in turn effects how heat is transferred from the heated surface to the surrounding fluid. Adjusting bubble characteristics/dynamics can have profound effects on the fluid's ability to quench the boiling surface. Harrison et al. previously noted that even a minimal amount of subcooling led to a dramatic reduction in fluid flow rate requirements to the boiling surface [11]. Gunther and Kreith noted that latent heat of vaporization during bubble formation only plays a small role in overall heat transfer from a superheated surface [9]. That indicates that convection heat transfer at the microlayer vapor/liquid/surface interface will be the dominant form of heat transfer during fully developed saturated boiling. Once subcooling is introduced, the thermal potential between the surface and the ambient is increased. With latent heat already playing a minority role in the heat transfer mechanism during saturated boiling, this difference is only amplified as the increase in the thermal potential drives even more heat to be transferred by convection/transient conduction mechanisms. The 5 °C subcooled condition data shown in Fig. 8 illustrate this dramatic drop in the coolant flow rate requirements corresponding to the definitive shift in the primary heat transfer mechanism at the surface from latent to convective/transient conduction. Using the ±0.5 °C spatial uniformity of temperature within the bath that the experimental facility's feedback loop and zone control provides, a 2.5 °C subcooled pool condition test was conducted showing a transition point between the dramatic shift indicated by current 5 °C data on Fig. 8 and previous 5 °C, 10 °C, 20 °C data [11] where latent heat has more of an effect and the surface begins to demand slightly more coolant for a given heat flux. Fundamentally, this conclusion is interesting in that it confirms through net coolant flow rate requirements that vaporization plays a small role in the energy balance at the surface under slightly subcooled pool boiling conditions. From a heat transfer mechanism however, the transient conduction and convection heat transfer modes would not be possible without the decrease in bubble departure diameter and consequent increase in bubble departure frequency associated with subcooled pool boiling heat transfer. Future work will use capacitance measurement in tandem with LIF techniques to quantify the void fraction at the surface to complete the conservation of mass analysis, but the current technique confirms fundamental expectations from a perspective that has not been examined with a dielectric fluid, namely net coolant flow rate requirements. This technique provides the foundation for a test standard that quantifies the relative convective/latent heat transfer relationship as a two-phase heat transfer surface performance parameter.

The coolant flow rates measured show that the convective/transient conduction heat transfer mechanism plays a much larger role than latent effects, especially as subcooling is increased. While it is difficult to model the effects of neighboring nucleation sites on a practical surface as coalescence and vapor plume distortion increase as heat fluxes reach

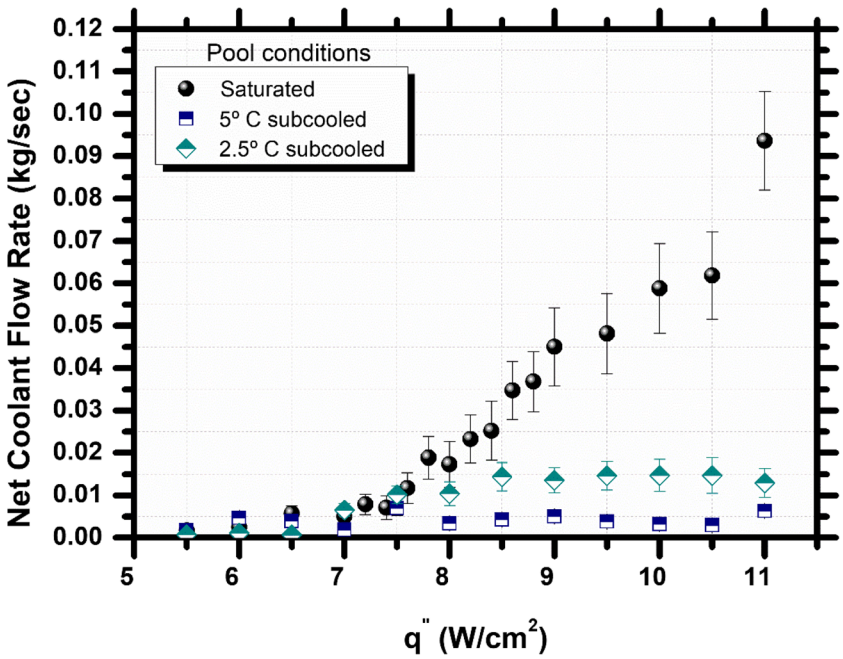

Fig. 8 Net coolant flow rate vs heat flux for saturated and subcooled pool conditions

conventional working limits, these effects can be removed if structured nucleation sites are introduced and heat fluxes are applied such that the boiling heat transfer performance mimics that of the isolated bubble regime[19, 22]. Near term future work will provide a model, based on accepted microlayer vapor/surface/liquid convection heat transfer theory [14], that will validate coolant flow rate requirements measured in the isolated bubble regime. While this isolated bubble regime typically functions at low heat fluxes, a fundamental model validating this experimental technique will provide greater confidence that it can be applied to any surface structure.

Recent advances in optimal co-design of thermal management solutions have centered around where passive and active components should be placed in order to maximize the reliability and efficiency of the final product in addition to minimizing the form factor and weight of the integrated solution [5, 7, 15, 21]. All of these co-design efforts have sought to quantify the effect of where and how fast the coolant enters the area around the heated element on thermal and electrical performance. An analysis of the vectors yielded by this technique can answer this question directly for any high heat flux surface cooled by two-phase heat transfer. For practical applications, the designer may want to know how fast the incoming fluid is approaching the boiling surface in order to assess the pressure drop around objects leading up to the heated surface and how nearby objects could be adjusted so as to reduce the pumping power needed to deliver coolant to, over, and past the powered component. A mean speed (magnitude of the velocity vector) value was calculated for all of the vectors contained within the full interrogation window highlighted in green in Fig. 5. As expected, the results of this analysis, shown in Fig. 9, with respect to input heat flux mirror closely the net coolant mass flow rate results of Fig. 8. This empirical data could be used in thermal management coolant flow optimization models as a free stream velocity requirement in computationally efficient reduced-order schemes. Data center optimization models do this often at the server node level within a large scale rack and/or multi-rack room [26].

In addition to knowing how fast the fluid is moving, it is of practical interest to know the net direction of the incoming fluid. Similar to the speed analysis data of Fig. 9, the average vector angle was calculated in the full interrogation boundary shown in green in Fig. 5. The change in angle with respect to varying heat flux over the full interrogation window is shown as solid line data on Fig. 10. The impact on this calculated angle with respect to the interrogation boundary was examined by calculating the average value over a smaller region. This smaller window boundary is shown in orange on the legend of Fig. 10. A reference coordinate system is also provided on Fig. 10 to show the direction of the resulting angle data with respect to the heated surface. Given the uncertainty bars shown on the plot, the interrogation boundary examined does not seem to have a statistically significant effect on the average approach angle of incoming fluid to the boiling surface. This is fundamentally expected as, at these interrogation boundary scales, there should be some degree of independence on the region selected via the continuity principle. At higher heat fluxes, those generally of most importance to the thermal engineer, subcooling does seem to draw the net approach angle more downward. This is an artifact of the significantly higher x-velocities in the saturated pool boiling case than in either of the subcooled cases examined. The higher

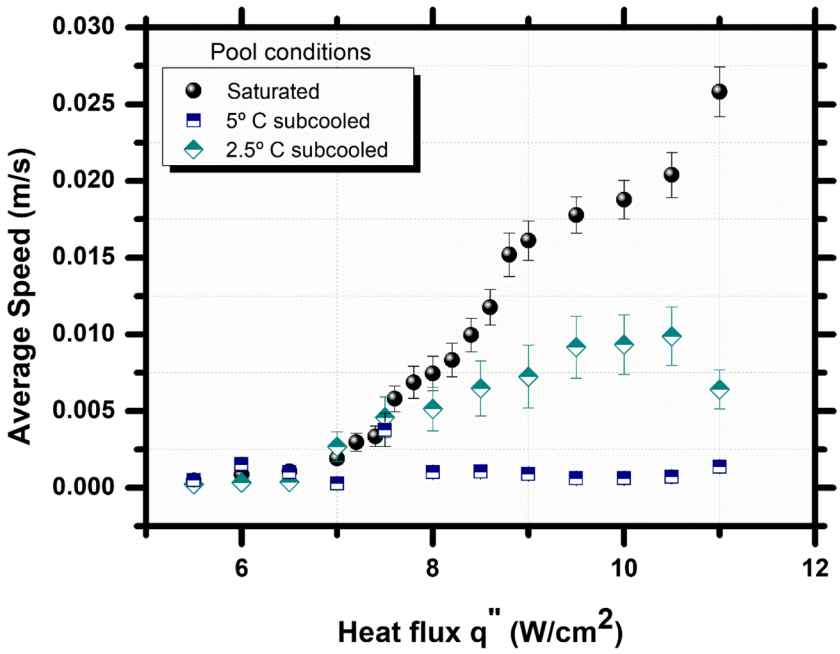

Fig. 9 Average speed of the incoming fluid to the boiling activity as input heat flux is varied

speeds (shown in Fig. 9) and net coolant flow rates (shown in Fig. 8) under saturated conditions are being supplied by fluid travelling horizontally into the interrogation boundary as the region is significantly more confined at the top (vapor/liquid free surface) and bottom of the boiling chamber than in the space extending normal to the periphery of the cylindrical control volume examined. Continuity mandates that these x-velocities increase at higher heat flux and the resultant approach angle adjusts accordingly over the three pool conditions examined as the magnitude of the coolant flow rate requirements reduce dramatically when subcooling is increased. At lower heat fluxes, the uncertainty begins to be on the order of the measurement taken for both the speed (Fig. 9) and net coolant flow rate (Fig. 8). Therefore, the projected uncertainty on the angle of approach mandates that only weak claims can be made on the impact of the heat flux and subcooling at these lower values. Generally, however, the data does support the fundamentally expected trend that as heat flux is increased, the fluid is pulled more horizontally in accordance with the surfaces demand for more fluid. While there are some interesting fundamental trends from the data presented in Fig. 10, it should be emphasized that the primary application of this approach angle data is more practical in nature. Similar to the speed data, it can be used in empirical reduced order models that seek to conclude what the impact is on pressure drop/coolant pumping requirements of slightly heated or completely passive neighboring components around an energy-dense surface cooled by two-phase heat transfer.

5 Conclusions

Utilizing two-phase fluorescent PIV, the authors have presented a novel way to quantify net coolant flow rates to boiling surfaces, particularly with a dielectric fluid. Axisymmetry on a circular boiling surface was used to construct an optimized control volume around a copper boiling surface. The vectors acquired through PIV were deconstructed around the periphery of this control volume to determine how much fluid was entering and leaving the area surrounding the boiling activity. Over a heat flux range of 5 W/cm^2 to 11 W/cm^2 (HTC's of 4.8 kW/(m^{2}K) to 8.8 kW/(m^{2}K)), net coolant flow rates varied from 1.7 g/s to 93.6 g/s, respectively with an average error in the flow rate measurement of 53.0% and 12.5% at minimum and maximum heat flux respectively under saturated pool conditions. The fundamental expectation of increased coolant flow rate requirements with increased power dissipation at the boiling surface was shown. Through these coolant flow rate measurements, it was shown that the dominant form of heat transfer changes dramatically with even the slightest amount of subcooling, transferring from latent/convective combination to a primarily convective/transient conduction combination. Future work will include increasing heat flux resolution, so the system can be tested closer to and with higher fidelity near the CHF condition where vapor coalescence and pockets of radiative heat transfer, which required no coolant to operate, begin to effect the overall heat transfer mechanisms. More fundamental expectations on the heat transfer mechanisms

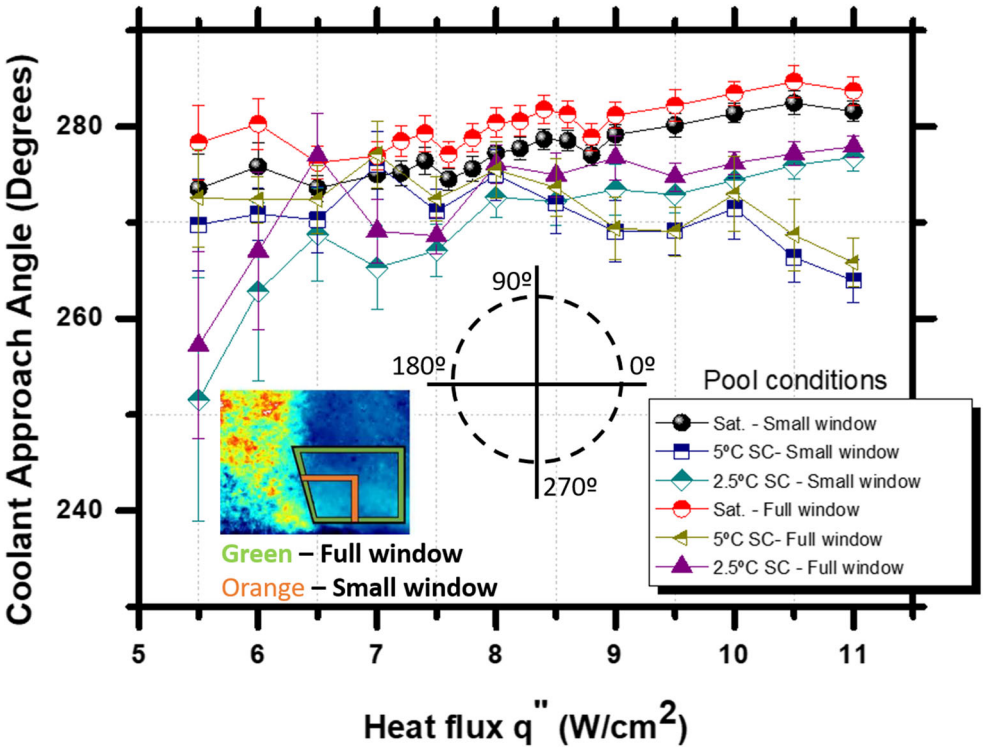

Fig. 10 Average approach angle of the coolant nearing the boiling surface as input heat flux is varied

near this point in the boiling curve and at the onset of fully developed boiling can be validated with this technique.

The authors believe that this empirical data can be employed in several practical applications for future models. Specifically, thermosiphons can be modelled with mass flow rate requirements as an empirical input. Multi-chip boards under two-phase liquid immersion cooling can also be modeled where fluid velocity boundary conditions are applied to the periphery of an energy dense chip. The ability to predict mass flow rates requirements, incoming coolant speeds, and approach angles as a function of heat flux can be used as a continuous empirical correlation in predictive reduced-order models across a range of expected operating conditions.

Acknowledgements Special recognition goes to FCT - Fundação para a Ciência e a Tecnologia for the IF 2015 recruitment program (IF 00810-2015 for they help in funding the collaboration efforts of Instituto Superior Tecnico of Lisboa and Oregon State University.

References

1. Adrian RJ (2005) Twenty years of particle image velocimetry. Exp Fluids 39(2):159–169
2. Campbell LA and Tuma P (2012) Numerical prediction of the junction-to-fluid thermal resistance of a 2-phase immersion-cooled IBM dual Core POWER6 processor. Semiconductor thermal measurement and management symposium (SEMI-THERM), march 18-22, San Jose, CA, pp. 36-44
3. Carey VP (2008) "Pool boiling," liquid vapor phase change phenomena, 2nd Ed. Taylor and Francis, New York, NY 2008:253–290
4. Demiray F, Kim J (2004) Microscale heat transfer measurements during Pool boiling of FC-72: effect of subcooling. Int J Heat Mass Transf 47:3257–3268
5. Eiland, R., Fernandes, J.E., Vallejo, M., Siddarth, A., Agonafer, D., and Mulay, V. (2017) Thermal performance and efficiency of a mineral oil immersed server over varied environmental operating conditions. Journal of Electronic Packaging, **139**(4), 041005-041005-9
6. Gerardi C, Buongiorno J, Hu L-W, McKrell T (2010) Study of bubble growth in water pool boiling through synchronized, infrared thermometry and high-speed video. Int J Heat Mass Transf 53: 4185–4192
7. Gess J, Bhavnani SH, Johnson RW (2015) Experimental investigation of a direct liquid immersion cooled prototype for high performance electronic systems. Transactions of the IEEE CPMT 5(10): 1451–1464
8. Gess J, Bhavnani S, and Johnson RW (2016) Single- and two-phase particle image Velocimetry characterization of fluid flow within a liquid immersion cooled electronics module. Journal of Electronic Packaging, **138**(4), pp. 041007-041007-11
9. Gunther FC, Kreith F (1956) Photographic study of bubble formation in heat transfer to subcooled water Progress report. 4-120, jet Propulsion Laboratory, Cal. Tech, 1956
10. Han C, Griffith P (1962) The mechanism of heat transfer in nucleate boiling. Technical report no. 7673-19, Department of Mechanical Engineering, Massachusetts Institute of Technology
11. Harrison M, Moita AS, Gess J (2018) A novel boiling heat transfer thermal efficiency parameter for microscale finned heat sinks using two-phase particle image Velocimetry. 19th international symposium on laser and imaging techniques to fluid mechanics, Lisbon, Portugal
12. Hsu YY (1962) On the size range of active nucleation cavities on a heating surface. J Heat Transf 84:207–213
13. International Technology Roadmap for Semiconductors (2015) International Technology Roadmap for Semiconductors 2.0 Executive Summary
14. Kim J (2009) Review of nucleate Pool boiling bubble heat transfer mechanisms. Int J Multiphase Flow 35(12):1067–1076
15. Kumar P, Sundaralingham V, and Joshi Y (2011) Effect of server load variation on rack air flow distribution in a raised floor data center. Semiconductor thermal measurement and management symposium (SEMI-THERM), march 20-24, San Jose, CA, pp. 90-96
16. Kurul N, Podowski M (1990) Multidimensional effects in forced convection subcooled boiling. Proceedings of the 9th international heat transfer conference, pp. 21-25
17. Lasance CJ, and Simons RE (2005) Advances in high-performance cooling for electronics. Electronics Cooling, 11(4)
18. Moffat RJ (1988) Describing the Uncertainties in Experimental Results. Experimental Thermal and Fluid Science 1(1):3–17
19. Moita AS, Teodori E, and Moreira ALN (2012) Enhancement of Pool boiling heat transfer by surface microstructuring. Journal of physics: conference series, **395**(1), 012175-012175-11
20. Parker JL, El-Genk MS (2005) Enhanced saturation and subcooled boiling of FC-72 dielectric liquid. Int J Heat Mass Transf 48(18): 3736–3752
21. Raciti A, Cristaldi D, Greco G, Vinci G (2015) Electrothermal PSpice modeling and simulation of power modules. IEEE Trans Ind Electron 62(10):6260–6271
22. Rahman MM, and McCarthy M (2015) Biotemplated nanostructures for enhancing CHF and HTC during Pool boiling. 9th international conference on boiling and condensation heat transfer, April 26-30, Boulder, CO
23. Ramakrishnan B (2014) Viability of server module thermal management using enhanced heat sinks and low global warming potential dielectric fluids. M.S. Thesis, Mechanical Engineering, Auburn University, Auburn, AL
24. Sathe MJ, Thaker IJ, Strand TE, Joshi JB (2010) Advanced PIV/LIF and Shadowgraphy system to visualize flow structure in two-phase bubbly flows. Chemical Engineering Science 65(8):2431–2442
25. Simons RE (1996) Direct liquid immersion cooling for high power density. Microelectronics Electronics Cooling, **2**(2)
26. Song Z, Murray BT, Sammakia B (2013) Airflow and temperature distribution optimization in data centers using artificial neural networks. Int J Heat Mass Transf 64:80–90
27. Teodori E, Moita AS, and Moreira ALN (2013a) Evaluation of Pool boiling heat transfer over micro-structured surfaces by combining high-speed visualization and PIV measurements. 10th international symposium on particle image Velocimetry - PIV13, Delft, the Netherlands
28. Teodori E, Moita AS, Moreira ALN (2013b) Evaluation of pool boiling heat transfer over micro-structured surfaces by combining high-speed visualization and PIV measurements. PIV 2013, Delft, the Nederlands
29. Westerweel J (1997) Fundamentals of digital particle image velocimetry. Meas Sci Technol 8(12):1379–1392